





RESEARCH ARTICLE | JUNE 03 2024

Dissolvable photovoltaic cells on hydrogel

Benxuan Li; Shijie Zhan; Zhe Li; Wenlong Ming; Gehan A. J. Amaratunga   ; Bo Hou  



APL Mater. 12, 061102 (2024)
<https://doi.org/10.1063/5.0197820>



APL Quantum
First Articles Online
No Article Processing Charges for Submissions
Through December 31, 2024
[Read Now](#)



Dissolvable photovoltaic cells on hydrogel

Cite as: APL Mater. 12, 061102 (2024); doi: 10.1063/5.0197820

Submitted: 14 January 2024 • Accepted: 6 May 2024 •

Published Online: 3 June 2024



Benxuan Li,^{1,2,3} Shijie Zhan,³ Zhe Li,⁴ Wenlong Ming,⁵ Gehan A. J. Amaratunga,^{2,6,a)}  and Bo Hou^{3,a)} 

AFFILIATIONS

¹International Collaborative Laboratory of 2D Materials for Optoelectronics Science and Technology of Ministry of Education, Institute of Microscale Optoelectronics, Shenzhen University, Shenzhen 518060, China

²Electrical Engineering Division, Department of Engineering, University of Cambridge, 9 JJ Thomson Avenue, Cambridge CB30FA, United Kingdom

³School of Physics and Astronomy, Cardiff University, The Parade, Cardiff CF24 3AA, United Kingdom

⁴School of Engineering and Materials Science (SEMS), Queen Mary University of London, London E1 4NS, United Kingdom

⁵School of Engineering, Cardiff University, The Parade, Cardiff CF24 3AA, United Kingdom

⁶Zhejiang University – University of Illinois Urbana Champagne Institute (ZJUI); School of Information Science and Electronic Engineering, Zhejiang University International Campus, Haining, China

^{a)}Authors to whom correspondence should be addressed: gajal@cam.ac.uk and houb6@cardiff.ac.uk

ABSTRACT

Solar energy is potentially the largest source of renewable energy for providing electrical power for human society. However, significant advances are required to make photovoltaic technologies have a low-carbon footprint in manufacture, be environmentally friendly at the end of their lives through recyclability, and be biodegradable. Here we report dissolvable organic photovoltaic devices based on poly(2-hydroxyethyl methacrylate), which show equal power conversion efficiency to their glass substrate-based counterparts. We use a novel method of including smectic liquid crystal (7-dioctyl[1]benzothieno[3,2-b][1]benzothiophene, C8-BTBT) as a crystal phase regulator in the heterojunction donor:acceptor polymer system to maintain the disposable organic solar cell efficiency without pre- or post-thermal annealing. The results show strong promise not only for more sustainable solar-cell fabrication but also as disposable and biocompatible solar cells for self-powered (energy harvesting) wearable and biomedical devices.

© 2024 Author(s). All article content, except where otherwise noted, is licensed under a Creative Commons Attribution (CC BY) license (<https://creativecommons.org/licenses/by/4.0/>). <https://doi.org/10.1063/5.0197820>

I. INTRODUCTION

Modern electronic systems are widely used in wireless sensing and intelligent monitoring with integrated communications in applications such as personal healthcare, environmental management, security provision, traffic control, and a host of others. The ability to harvest and store energy in these systems can allow them to have a longer and more robust operational lifetime.¹ Solar energy is the most abundant, sustainable, and cleanest available energy source, but challenges remain when it comes to converting it to electrical power through photovoltaics (PVs) related to the limits of efficiency and cost of materials and energy required for cell manufacture. In addition, recyclability and biocompatibility/degradability are also aspects of PV cells that are currently of concern. During the past two decades, organic solar cells (OSCs) have emerged as promising

third-generation photovoltaic devices due to their low cost of manufacture associated with solution processing at low temperatures. (A table of symbols is provided in Table S1.) Power conversion efficiencies (PCEs) at AM1.5 solar illumination have improved over time, currently reaching 19.03%.² The indoor cell record efficiency has reached 36%.³ While their suitability for bulk terrestrial power generation is still limited due to their limited lifetime under atmospheric conditions, they are a favored option for applications in which energy generation from light in indoor environments is needed.⁴

In terms of the biocompatibility and recyclability of PV cells, research is in the initial stages. For conventional silicon-based cells/panels, aluminum, glass, and silicon can be recycled through thermal and chemical methods,⁵ while valuable metal elements such as silver, copper, and tin can, in principle, be extracted and reused by chemical precipitation, chemical coagulation, electrochemical

separation, and biosorption.^{6–8} In OSCs, polyethylene terephthalate (PET) and polyethylene naphthalate (PEN) are two polymers widely used as lightweight and flexible substrates in flexible electronics.⁹ However, from a life-cycle perspective, these petroleum-based substrates are less attractive than other inexpensive, environmental-friendly, and recyclable substrate materials such as cellulose and paper.^{10,11} But celluloses have low solubility, while the surface roughness of papers limits their suitability for thin film OSCs.¹² As alternatives, polymers such as poly(vinyl alcohol) (PVA), poly(lactic acid) (PLA), poly(ethylene glycol) (PEG), and polydimethylsiloxane (PDMS) have been introduced as substrates for organic and thin film electronics, but their biodegradability and biocompatibility are still under optimization.^{13,14} Recently, hydrogels have attracted considerable attention as another candidate for flexible electronics, which have the advantages of unique softness, outstanding flexibility, and exceptional biocompatibility. For instance, poly(2-hydroxyethyl methacrylate) (PHEMA)-based hydrogels have been widely used in controlled drug release systems, contact lenses, and soft robotics.^{15,16} However, to the best of our knowledge, PHEMA hydrogel has not been used as a substrate material in OSCs as yet. Furthermore, the application of PHEMA may enable OSCs to be more environmental-friendly in terms of sustainable end-of-life management.

Since the mid-1990s, many operating principles of OSCs have been elucidated from studying what is now the classic, poly-(3-hexylthiophene):[6,6]-Phenyl-C₆₁-butyric acid methyl ester (P3HT:PCBM) distributed heterojunction system. Adding a complementary additive to construct a ternary solar cell is an approach to improving the performance of classical OSCs. Polymers and oligomers have been used as additives and, more recently, liquid crystal (LC) molecules in OSCs.^{17,18} We introduce here a smectic LC 2,7-Dioctyl[1]benzothieno[3,2-b][1]benzothiophene (C8-BTBT) into the P3HT:PCBM system to realize ternary OSCs. The LC enables the optimization of polymer crystallization at room-temperature (RT), which enables PHEMA hydrogel-based OSC devices to be fabricated under low-temperature conditions. Parameters of the fabricated OSCs with different weight fractions of C8-BTBT loadings are presented. Spectroscopic and crystallographic analysis of active layer films reveals the interplay between polymer ordering, crystallinity, morphology, and device performance. Reproducible surface morphology is also obtained by adjusting different photopolymerization times. The solubility and disposability of OSCs on hydrogels are evaluated using different polar and non-polar solvents. The results confirm that PHEMA-based OSCs can be easily recycled using a commonly used solvent.

II. MATERIALS AND METHODS

A. Materials

The poly(2-hydroxyethyl methacrylate) (PHEMA) hydrogel was synthesized using 2-hydroxyethyl methacrylate (HEMA, Sigma-Aldrich, 97%) as a monomer and ethylene glycol dimethacrylate (EGDMA, Sigma-Aldrich, 98%) as a crosslinking agent. The photoinitiator diphenyl(2,4,6-trimethylbenzoyl)phosphine oxide (TPO, Sigma-Aldrich, 97%) served as an initiator for polymerization. The Al 4083 poly(3,4-ethylenedioxythiophene):polystyrene sulfonate (PEDOT:PSS) solution from Ossila Ltd. P3HT was purchased

from Rieke Metals (LLC, 4002-E Mw 50 000–70 000 and regioregularity $\geq 90\%$) and PCBM was from Ossila Ltd. (purity $> 99\%$). C8-BTBT was purchased from Sigma-Aldrich (purity $\geq 99\%$).

Several groups of polar and non-polar solvents were used to determine the solubility of PHEMA and the disposability of PHEMA-based OSCs. Solvents are hexane (Sigma-Aldrich, purity $\geq 95\%$), tetrahydrofuran (THF, Sigma-Aldrich, purity $\geq 99\%$), toluene (Sigma-Aldrich, purity $\geq 99.5\%$), acetone (Sigma-Aldrich, purity $\geq 95\%$), 2-propanol (Sigma-Aldrich, purity $\geq 99.5\%$), dichloromethane (Sigma-Aldrich, purity $\geq 99.8\%$), chloroform (Sigma-Aldrich, purity $\geq 99.5\%$), formamide (Sigma-Aldrich, purity $\geq 99.5\%$), dimethylformamide (DMF, Sigma-Aldrich, purity $\geq 99.8\%$), N-methyl-2-pyrrolidone (NMP, Sigma-Aldrich, purity $\geq 99.5\%$) and dimethyl sulfoxide (DMSO, Sigma-Aldrich, purity $\geq 99.7\%$). The solubility of PHEMA thin films was first explored using these solvents, and then PHEMA-base OSCs were dissolved in those solvents that can dissolve PHEMA thin films.

B. Sample preparation

1. Synthesis of hydrogel substrates

For the synthesis of PHEMA hydrogels, 6 μ l EGDMA and 13 mg TPO were dissolved in 6 ml HEMA to obtain a 10 ml precursor solution, followed by adding 4 ml deionized water and carefully degassing the yield solution with nitrogen for 1 h. After degassing, the precursor solution was injected into a 2-in. Petri dish, which was followed by ultraviolet (UV) photopolymerization in a UVP crosslinker (Analytik Jena). Apart from exploiting a glass Petri dish for PHEMA photopolymerization, the solution was also injected into the mold consisting of two glass plates, wherein the monomer solution was UV photopolymerized at a different time using the same UVP crosslinker. Note that these two approaches can result in different photopolymerization results for PHEMA, especially differences in thin film morphology. We will compare and discuss differences in detail in Sec. III A. Finally, the prepared PHEMA hydrogel was immersed in distilled water (DI water) for 24 h, resulting in a fully swollen state for the next step of deposition.

2. Deposition of indium tin oxide (ITO)

ITO as a hole transport layer was deposited on prepared PHEMA substrates through a mask in a radio frequency (RF) sputtering system. In the ITO sputtering process, RF power and Argon (Ar) flow were adjusted to 75 W and 30 sccm without using a heater under the substrate, with deposition pressure in the chamber set at around 7.7×10^{-6} Torr for a roughing pump and then down to 4×10^{-6} Torr during deposition.

3. Fabrication of organic solar cells

The PEDOT:PSS solution was filtered prior to use through a 0.45 μ m hydrophilic polyvinylidene fluoride (PVDF) filter. The pre-cleaned substrates were processed by ozone plasma for 5 min to remove all organic residues and increase surface hydrophilicity. Following that, the filtered PEDOT:PSS solution was extracted via a syringe to cover the entire substrate and spun at 3500 rpm for 40 s to produce a hole-only transfer layer of ~ 40 nm thickness. After spin-coating was finished, substrates were heated on the hotplate at 140 °C for 10 min to form better morphological thin films.

Prior to deposition of the active layer, 15 mg of P3HT as donor material and 12 mg of PCBM as acceptor material were dissolved in chlorobenzene to prepare a polymer solution and stirred on a hotpot for 24 h at 50 °C in the glovebox to get better polymer dispersion. C8-BTBT was dissolved in chlorobenzene and added to P3HT:PCBM solutions with 5 wt. % of C8-BTBT loading. After proper stirring, mixed polymer solutions were spin-coated on top of the PEDOT:PSS layer at 1000 rpm for 45 s to obtain a thickness of 120 nm, and then samples were placed in the glovebox without thermal annealing. Finally, cathode electrodes were formed onto active layers by evaporating ~100 nm thickness of aluminum (Al) in the thermal evaporator, in which substrates were placed in the chamber with a deposition mask covering the desired thin film active region, and air pressure in the chamber was kept at 2×10^{-6} Torr.

C. Thin-film characterization and device characterization

1. PEHMA morphology characterization

The surface morphology of PHEMA thin films was investigated using scanning electron microscopy (SEM, FEI Magellan 400). Before SEM measurement, samples were sputtered with ~10 nm thickness of gold to increase surface conductivity. The 2D surface morphology of crosslinked PHEMA was investigated by the VEECO WYKO NT9100 Optical Profilometer, shown in Fig. S2.

2. ITO thin-film characterization

The sputtering period is set to be 600 s to achieve ~100 nm thickness of ITO, and the thickness of ITO was measured via a Bruker Dektak XT stylus profilometer to confirm ITO deposition results. In addition, a resistance of $45 \Omega \text{sq}^{-1}$ was obtained on coated-ITO via a four-probe measurement. Though this value is 4–5 times higher than commercial ITO-pattern substrates, it is still within an acceptable range for a bio-compatible organic solar cell.

3. Device characterization

The electrical behavior of organic solar cells (OSCs) was measured under both dark and simulated illumination conditions. A solar simulator was used to simulate the AM 1.5G spectrum, with light intensity accurately measured at 100 W cm^{-2} by a solar meter and calibrated using a RERA SOLUTIONS silicon reference cell (RQS4695) before each measurement. Both AM 1.5G $J-V$ curves and dark $J-V$ curves were recorded using a Keithley 4200-SCS semiconductor characterization system. From these statistics, short-circuit current (J_{sc}), open-circuit voltage (V_{oc}), fill factor (FF), and power conversion efficiency (PCE) can be calculated, respectively. All $J-V$ measurements were performed in an ambient atmosphere at room temperature.

III. RESULTS AND DISCUSSION

A. Optimisation of PHEMA hydrogel substrates

The schematic representation of the PHEMA hydrogel fabrication process using UV illumination is illustrated in Fig. 1(a). The process can be controlled by varying UV light intensity, exposure time, concentrations of photoinitiators, and monomers (the photopolymerization procedure of PHEMA is given in Fig. S1). A glass mold was employed to confine the injected PHEMA solution

inside a flat glass mold in two dimensions (z-axis direction and x/y direction). A smooth PHEMA surface is obtained as the hydrogel is compressed by a rigid flat glass, limiting surface wrinkling during photopolymerization. Figures 1(b) and 1(c) present images of crosslinked PHEMA thin film before and after peeling off from the glass mold. From both photos, very good transparency of crosslinked PHEMA thin films can be observed. The thickness of the glass mold controls the thickness of the PHEMA thin film, which is 1.1 mm in our case.

In addition, it can be seen from Fig. 1(d) that PHEMA thin film exhibits >85% transmittance in the visible spectrum. With ~100 nm ITO coated on the PHEMA thin film, the substrate offers comparable transmittance to the commercial ITO-coated glass substrate (with marginally higher transmission in the 400–600 nm range). Therefore, differences in light absorption will have negligible influence on the photovoltaic performance when comparing soft ITO-coated PHEMA thin films with rigid commercial ITO-coated glass substrates. The flexibility of PHEMA thin films is shown in video S1, where PHEMA thin film is installed and bent on our designed bending machine.

The surface morphology of mold-fabricated PHEMA thin films was examined by SEM at two different magnifications and analyzed using image processing software, as shown in Fig. 2.

As shown in Fig. 2, it is seen that surface wrinkling occurs independently of the crosslinking time employed. But a significant difference can be observed in terms of wrinkling width. In addition to wrinkle structure, the distribution of wrinkle width over the surface also differs significantly. In the case of 10-min crosslinked PHEMA, the wrinkle width is larger than for the other three cases, with the normal distribution of width exhibiting a mean and standard deviation of $2.24 \pm 0.82 \mu\text{m}$. When photopolymerization and crosslinking durations are extended to 20 and 30 min, surface wrinkles become flatter, leading to average wrinkle widths of $1.41 \pm 0.45 \mu\text{m}$ and $0.99 \pm 0.23 \mu\text{m}$, respectively. Interestingly, the PHEMA sample processed for 40 min exhibits a larger wrinkle width than the 30-min samples, with an average of $1.12 \pm 0.41 \mu\text{m}$. It has been reported previously that fast contraction may constrain wrinkle length into a mixture of different populations instead of one single wrinkle, and that a short molecular weight crosslinking agent leads to the generation of a dense network with poor swelling capability.¹⁹ As shown in Fig. S2, when 100 nm of ITO is sputtered onto PHEMA films crosslinked with different durations of 10, 20 and 30 min, surface roughness variations with root mean square roughness (Rq) decreasing from 9.82 to 2.85 and 1.62 nm, respectively, are observed. But the Rq value increases to 4.43 for the 40-min crosslinked PHEMA film. The swelling capability of PHEMA thin films is dependent on UV photopolymerization duration, and consequently, a 30-min treatment results in thin films with a narrow and minimally distributed wrinkle width. This, in turn, is beneficial for smooth ITO layer deposition and subsequent device performance.^{20,21}

B. Organic solar cells improved by smectic liquid crystal incorporation

Since the glass transition temperature of PHEMA is reported to be 113 °C,²² a moderate-to-low-temperature fabrication process is required for thin film electronic/optoelectronic devices that have PHEMA as a substrate. Moreover, thermal annealing has

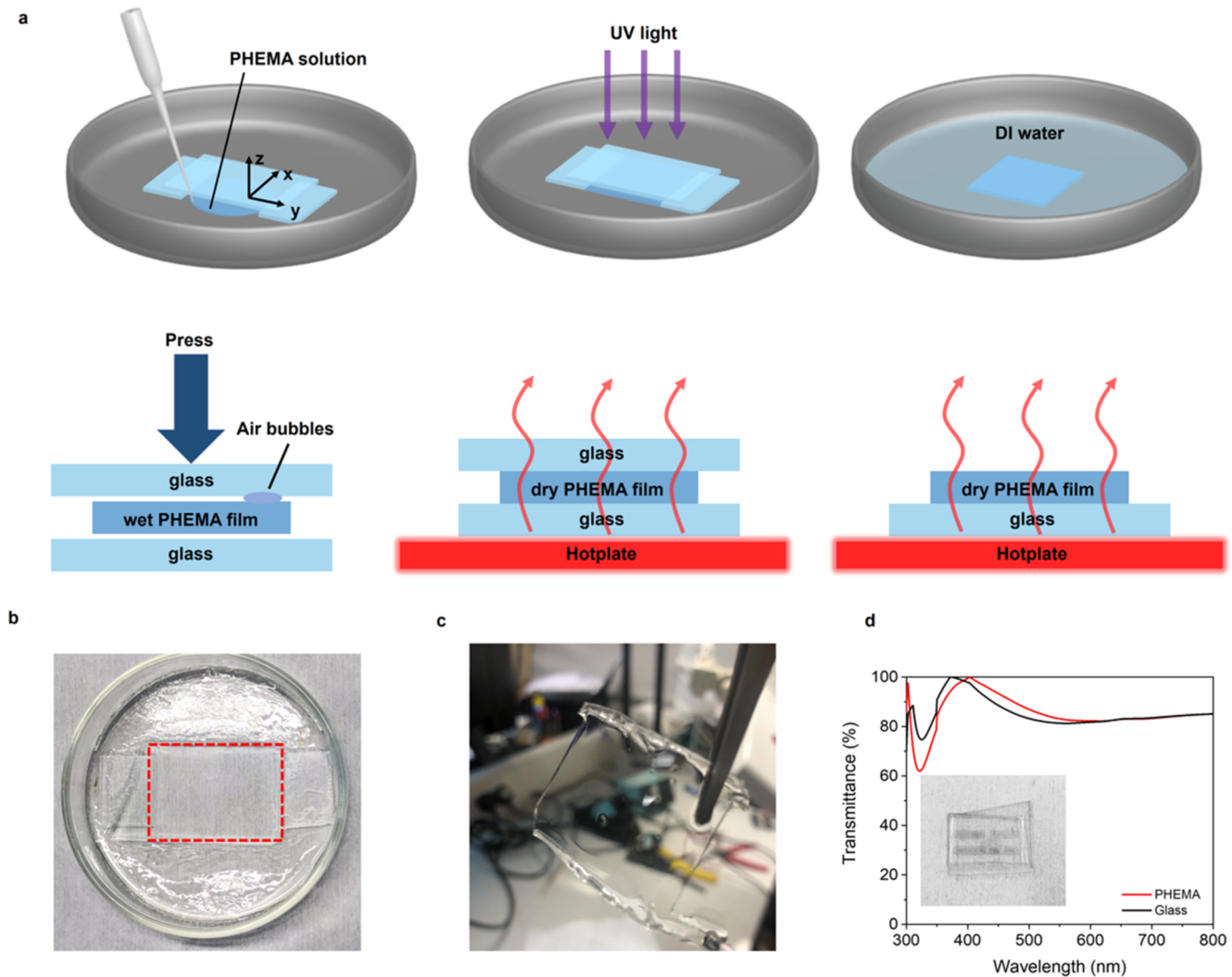


FIG. 1. (a) Schematic of the PHEMA film fabrication process. (b) Image of PHMA thin film photopolymerized inside a glass mold (highlighted by a red dashed line). (c) Photo of PHEMA thin film peeled off from the mold. (d) Transmittance spectra of ITO-coated PHEMA thin film and the commercial ITO-coated glass substrate. (Insert the photo of the ITO-coated PHEMA substrate.)

been commonly applied to improve organic solar cell performance through improved polymer crystallinity and phase separation.^{23,24} To overcome the limitations of annealing temperature for OSCs on PHEMA, we introduce a small liquid-crystal molecule C8-BTBT, into the P3HT:PCBM system to improve anisotropic organic crystallization without thermal annealing.

The C8-BTBT molecule consists of two thiophene rings and adjacent benzene rings connected with alkyl side chains, which enable its liquid crystal behavior as the rigid part (thiophene rings) favors both orientational and positional order while the rest of the molecule is flexible.²⁵ Differential scanning calorimetry (DSC) thermogram for C8-BTBT identified a sharp endothermic peak associated with the transformation from solid-state to liquid crystalline (Cr) at 109.98 °C and to a smectic A (SmA) phase at 125.62 °C, close to other reported values.^{26,27} [as shown in Fig. 3(a)] The

liquid crystallinity nature of the C8-BTBT molecule can be further verified by polarized optical microscopy (POM), as shown in Fig. S3. POM images of P3HT:PCBM:C8-BTBT thin films are shown in Fig. S4.

The application of C8-BTBT smectic liquid crystal in the P3HT:PCBM heterojunction system was investigated through fabricating OSCs with different C8-BTBT loadings. The configuration of the fabricated OSCs, with the chemical structures of P3HT and C8-BTBT, is shown in Fig. 3(b). Furthermore, the evolution of J_{sc} , V_{oc} , FF, PCE, R_s , and R_{sh} is provided in Figs. 3(c)–3(e), respectively, as a function of C8-BTBT loading. The J_{sc} , FF, and PCE of standard cells improve from 1.82 mA cm⁻², 0.32%, and 0.38% without thermal annealing to 2.40 mA cm⁻², 0.36%, and 0.56% with 5 wt.% C8-BTBT loaded, respectively.

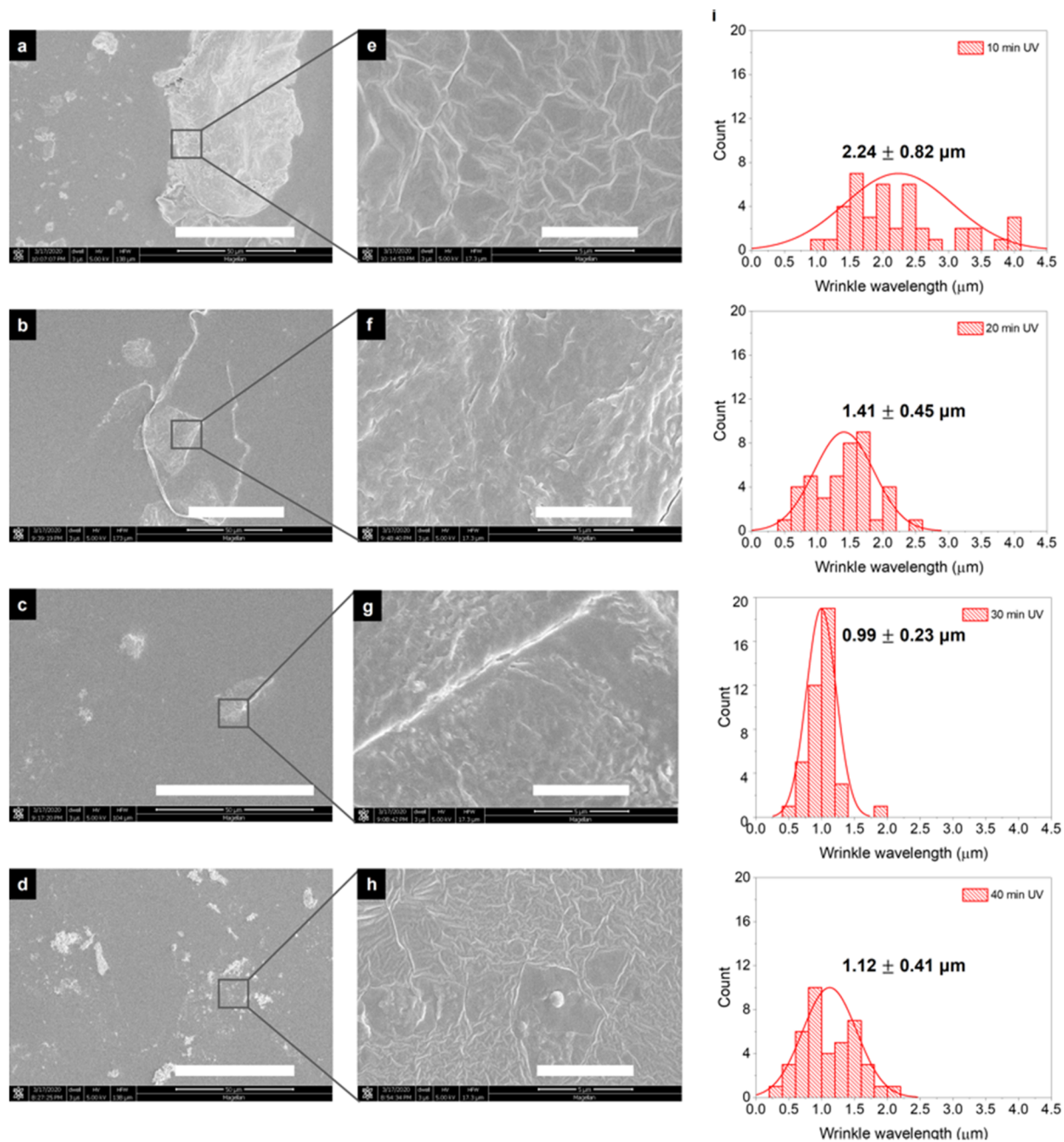


FIG. 2. SEM images of PHEMA thin films photopolymerized at different times under a UV crosslinker using glass molds. (a) and (e) 10-min photopolymerization. (b) and (f) 20-min photopolymerization. (c) and (g) 30-min photopolymerization. (d) and (h) 40-min photopolymerization. The scale bar in (a)–(d) is 50 μm and (e)–(h) 5 μm . (h) Histograms of wrinkle width for each case.

An increasing trend for J_{sc} , FF, and PCE (AM1.5) is seen with more C8-BTBT loading ratios. In addition, the best values are achieved when it reaches 5 wt. % loading of C8-BTBT, while large decreases occur for 10 wt. % C8-BTBT loading.

The improvement of device performance with the incorporation of C8-BTBT may be ascribed to the self-assembled liquid crystalline molecules inducing greater polymer crystallinity and a better interpenetrating network. The normalized UV-vis

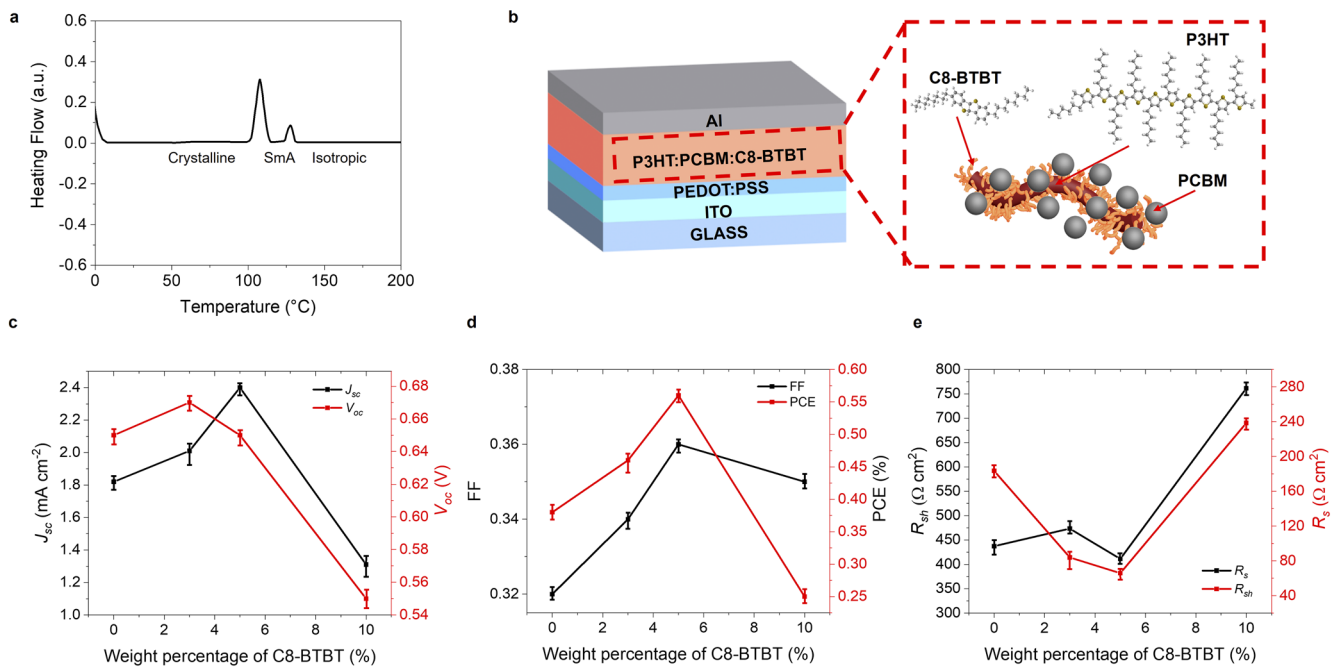


FIG. 3. (a) DSC result of C8-BTBT. (b) Schematic of OSC architecture. (c)–(e) Evolution of P3HT:PCBM:C8-BTBT-based OSC characteristics with a C8-BTBT weight percentage difference. (c) J_{sc} and V_{oc} . (d) FF and PCE. (e) R_s and R_{sh} .

absorption spectra of P3HT:PCBM with loading of C8-BTBT liquid crystal molecules are given in Fig. S5. From a P3HT-based perspective, the measured absorption spectra consist of two parts: a low-energy region that features the vibronic structure of aggregates in P3HT and a high-energy region that is attributed to unaggregated P3HT chains.²⁸ From the PCBM-based perspective, the peak centered at around 335 nm is a typical absorption of PCBM, and its position will shift slightly if the dimensions of PCBM domains vary.²⁹ The spectroscopic shifts can be observed when certain weight fractions of C8-BTBT liquid crystal molecules are incorporated into P3HT:PCBM to form P3HT:PCBM:C8-BTBT ternary blends, indicating stronger π - π^* interaction and closer π - π stacking in the P3HT:PCBM blends. This in turn facilitates better charge carrier mobility.^{30,31} According to Spano's model, the ratio of A_{0-0} and A_{0-1} absorbance peaks is correlated with the free exciton bandwidth of aggregates W , and the energy of the main intramolecular vibration E_p coupling to the electronic transition is given by the expression: $A = \frac{A_{0-0}}{A_{0-1}} \approx \left(\frac{1-0.24W/E_p}{1+0.073W/E_p} \right)^2$.^{27,29} Using the A_{0-0} and A_{0-1} peak values from Fig. S5 and assuming the C=C symmetric vinyl stretch at 0.18 eV dominates during coupling to the electronic transition,^{32,33} then using $E_p = 0.18$ eV, exciton bandwidth W can be obtained. When interchain order is assumed to be identical and W is associated with polymer conjugation length and intrachain order in the blended thin film, an increase in polymer conjugation length and order will result in a decrease in W .³⁴ Put differently, variation in W is an indication of conjugation level and ordering inside blended solid-state polymer films. Calculated W values are shown in

Fig. 4(a), where a clear drop in W value can be witnessed compared to the pristine P3HT:PCBM sample when the C8-BTBT ratio gradually rises, which is in line with the evolution of J_{sc} . Consequently, the spectroscopic behavior in P3HT:PCBM:C8-BTBT thin films is in agreement with device electrical characteristics, with the W value indicating the correlation of C8-BTBT loading and ordering of the polymer.

To further understand the morphology and crystallinity of active layers and confirm the effect of C8-BTBT on the ordering and crystallinity of P3HT, XRD measurements of P3HT:PCBM thin films with and without C8-BTBT were performed. The XRD spectra are presented in Fig. 4(b) and Fig. S6. There are two peaks at 5.35° and 10.8°, which are assigned to the (100) and (200) diffractions of P3HT crystallites.³⁵ For pristine P3HT:PCBM samples, the position of the diffraction peaks is fixed at the same angles independent of annealing temperature variation, while intensity at (100) increases with higher temperature. In contrast, the (100) peak in P3HT:PCBM:3 wt. % C8-BTBT and P3HT:PCBM:5 wt. % C8-BTBT samples shifts to a larger angle of 5.46°, indicating closer intraplanar spacing of P3HT when LC is incorporated.³⁶ In addition, the highest intensity at (100) occurs for the P3HT:PCBM: 5 wt. % C8-BTBT thin film. This can be associated with the highest crystallinity and is supported by spectroscopic and device performance data. With the incorporation of C8-BTBT molecules, two additional diffraction peaks are observed at 2θ values of 6.28° and 9.11°, which are attributed to the (002) and (003) planes of C8-BTBT crystals, respectively.³⁷

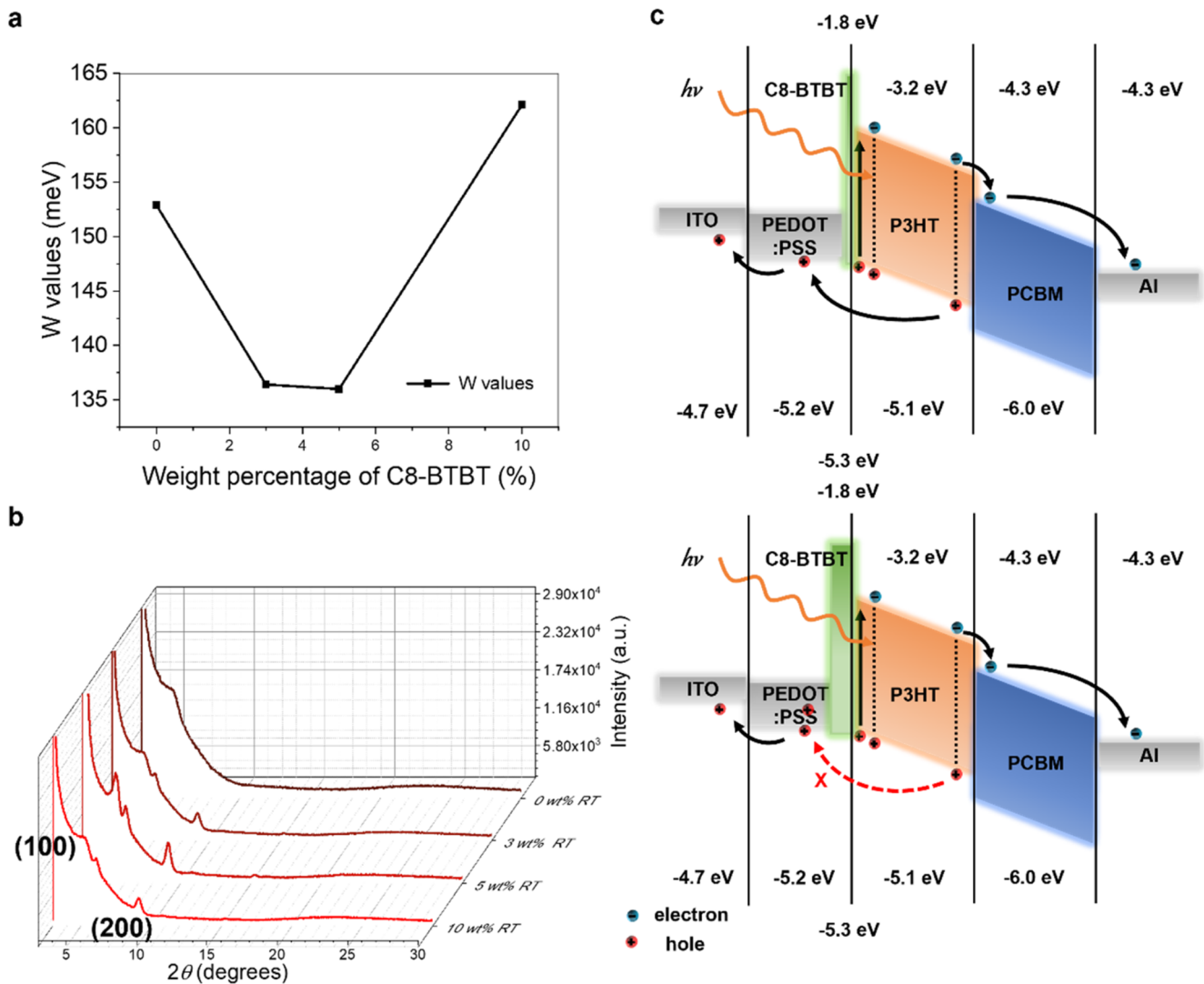


FIG. 4. Evolution of P3HT:PCBM:C8-BTBT sample characteristics with C8-BTBT weight percentage difference (a) Exciton bandwidth W of ordered aggregates. (b) XRD results. (c) Energy diagram with a different amount of C8-BTBT.

In the ternary blend with the highest weight fraction of C8-BTBT, P3HT:PCBM:10 wt. % C8-BTBT, the (100) and (200) diffraction peaks of P3HT are diminished, but the two C8-BTBT diffractive peaks show a noticeable intensity. This indicates that the crystallinity of P3HT is suppressed by C8-BTBT having a larger fraction of molecules. The decreased photovoltaic performance for P3HT:PCBM:10 wt. % C8-BTBT-based OSCs is, therefore, to be expected.

AFM was also used to investigate the effect of C8-BTBT on the morphology of P3HT:PCBM thin films, thereby linking morphology changes with performance in P3HT:PCBM:C8-BTBT ternary OSCs. With the incorporation of C8-BTBT LC molecules,

ternary thin films appear to have a smoother surface, as shown in Figs. S7(a)–S7(d), corresponding to 3 wt. % C8-BTBT loading, and Figs. S7(d)–S7(f), corresponding to 5 wt. % C8-BTBT loading. An increase in C8-BTBT concentration to 10 wt. % leads to greater roughness of the ternary thin films [Figs. S7(g)–S7(i)]. The terrace-like structures that are clearly observed could be an indication of surface phase segregation of C8-BTBT molecules.²⁷ It has been reported that the crystallization of P3HT chains occurs before the diffusion of PCBM to nucleation sites, where PCBM agglomerations develop.³⁸ Notably, ternary thin films with 3 and 5 wt. % C8-BTBT incorporation tend to exhibit smaller rms values of surface roughness, which indicates that loading of C8-BTBT molecules

facilitates crystallization of P3HT but simultaneously prevents part of the PCBM from moving to the surface. Nevertheless, when the loading ratio increases to 10 wt. %, abundant C8-BTBT molecules themselves start to aggregate at the surface and subsequently become barriers and traps that negatively influence the interface and consequently device performance. Energy diagrams of P3HT:PCBM:CB-BTBT-based solar cells are depicted in Fig. 4(c). Energy level data are from previous reports.^{39–41} Accordingly, it is possible to surmise that when the C8-BTBT loading ratio is in the range 3–5 wt. %, only a thin layer of C8-BTBT is soft-coated between P3HT:PCBM, and this thin layer will not prohibit the hole transfer pathway from P3HT to PEDOT:PSS and electron transfer from P3HT to PCBM. At higher concentrations of C8-BTBT, a thicker layer that suppresses efficient hole transfer inside the blend is present.

The beneficial effects of thermal treatment on P3HT:PCBM solar cells have previously been reported and verified.^{42–44} We investigated OSCs with three weight fractions of C8-BTBT with and without pre-thermal annealing treatment (shown in Figs. S8 and S9). The J_{sc} in samples with 0, 3, and 5 wt. % C8-BTBT increases considerably with successive temperature increments from room temperature (RT) to 60 and 120 °C, while J_{sc} values in cells with 10 wt. % C8-BTBT only exhibit a moderate rise. More specifically, OSCs with 3 and 5 wt. % C8-BTBT reach the maximum J_{sc} at 120 °C, whereas the maximum J_{sc} appears at 150 °C in both pristine and 10 wt. % C8-BTBT loading OSCs. This difference in J_{sc} is presumed to be associated with C8-BTBT thermodynamic behavior, as the molecule stays in a liquid crystalline state at around 120 °C. On the other hand, V_{oc} , FF, and PCE do not increase monotonically with annealing temperature.

Considering R_s , R_{sh} , and FF of pn-junction solar cells, it can, therefore, be expressed as the following semiempirical equations: $FF = FF_s \left(1 - \frac{v_{oc} + 0.7}{v_{oc}} \frac{FF_s}{R_{sh}} \right)$, where FF_0 is the fill factor of an ideal solar cell and FF_s characterizes the fill factor of solar cells that only consider R_s , $\left\{ FF_0 = \left(\frac{v_{oc} - \ln(v_{oc} + 0.72)}{v_{oc} + 1} \right) \right\}$, $FF_s = FF_0 (1 - R_s)$.⁴⁵ Therefore, R_s becomes one of the limiting factors of FF in solar cells. The correlation of R_s and R_{sh} and C8-BTBT weight percentage is given in Fig. 3(e), exhibiting an overall decreasing trend across all samples, which is in good accordance with the FF evolution. Not surprisingly, 10 wt. % C8-BTBT cells display the highest R_s among all samples, and their value rises to as high as 238.5 $\Omega \text{ cm}^2$ (average value) at RT conditions without any thermal annealing process. As shown in Fig. 3(e), the highest R_{sh} of 761.481 $\Omega \text{ cm}^2$ (average value) can be found inside 5 wt. % C8-BTBT devices processed at 120 °C, which simultaneously achieves the highest FF of 0.55. Nevertheless, there is no strong inverse correlation between R_{sh} and FF. In this regard, it seems that FF is more sensitive to a change of R_s rather than R_{sh} , which suggests $FF \sim FF_s$ for the relative values of R_s and R_{sh} .^{46,47}

C. Dissolvable photovoltaics enabled by C8-BTBT and PHEMA hydrogel substrates

As shown in Fig. 5(a), PHEMA-based OSC with 5 wt. % C8-BTBT loading performs with V_{oc} of 0.567 V, J_{sc} of 1.50 mA cm^{-2} , FF of 35.51%, and PCE of 0.31% under AM 1.5 G illumination, compared with 0.573 V_{oc} of 0.573 V, J_{sc} of 1.17 mA cm^{-2} , FF of

25.83%, and PCE of 0.17% in a device with a pristine P3HT:PCBM active layer. It should be noted that, compared with conventional P3HT:PCBM OSCs, our device exhibits less desirable performance. This is attributed to two reasons: (i) the sputtered ITO on PHEMA exhibits relatively higher resistance; (ii) our device is not processed with any post-optimization process such as thermal annealing or solvent annealing. Consequently, a 28.2% increase in J_{sc} is achieved with 5 wt. % C8-BTBT loading in P3HT:PCBM, which is in good agreement with our rigid devices. However, values of FF and PCE are low, indicating high series resistance, which is attributed to the absence of any annealing process and ITO sputtering (324.53 $\Omega \text{ cm}^{-2}$ for a pristine P3HT:PCBM device and 228.93 $\Omega \text{ cm}^{-2}$ for a 5 wt. % C8-BTBT loading device). Log-linear light and dark J - V characteristics of pristine P3HT:PCBM and P3HT:PCBM:5 wt. % C8-BTBT devices are shown in Figs. 5(b) and 5(c), respectively. In Fig. 5(d), a bent PHEMA-based OSC exhibits the flexibility of the device.

The environmental-friendly disposability of used PV cells is one of the major concerns for sustainable management of photovoltaics.⁴⁸ In this regard, we first explore the solubility of PHEMA thin film by testing several groups of commonly used solvents. PHEMA is insoluble in hexane, partly soluble in toluene, and fully dissolved in DMSO (Figs. S10 and S11). We also tried other commonly used solvents and divided these solvents into three classifications according to their solubility in PHEMA thin films. Therefore, it is presumed that both dipole moment and solubility in water influence PHEMA dissolution, since solvents with higher polarity (around 4.0 D) and good water solubility tend to dissolve PHEMA thin films more completely. Given that PHEMA is intrinsically hydrophilic, good water solubility facilitates the formation of hydrogen bonding and, therefore, may help to dissolve PHEMA.⁴⁹ In addition, according to the chemists' adage, "like dissolves like," high-polarity solvents may readily dissolve polar solutes. Consequently, the observed solvent-dependent solubility of PHEMA thin film can be explained by a coordinating effect of both solvent polarity and water solubility. Figure 5(e) displays time-lapse images that record the solubility of a fabricated cell in DMSO. It can be noted that the active layer, metal electrode, and ITO layer are easily separated from the substrate within 5 min. (The tube was shaken by hand to accelerate the disintegration process.) In addition, it takes around 5 days to dissolve the entire PHEMA-based OSCs, with only a small amount of PHEMA residue on the glass stand and solid waste left at the bottom of the tube. Note that both P3HT and PCBM have high solubility in halogenated aromatics and halogenated alkane solvents but relatively poor solubility in alcohols and polar solvents.⁵⁰ Therefore, P3HT and PCBM become sediment in the DMSO and can be filtered out and collected. Compared to other methods such as burning,^{51–53} leaving a residue of ashes and haze, the ability to dissolve OSCs in a solvent is more desirable as it results in a lower carbon footprint based on life-cycle assessment (LCA) and techno-economic analysis (TEA).^{53,54} Besides, the use of highly toxic aromatic solvents that are hazardous for humans and the environment is avoided.^{52,55} Considering its environmental friendliness, DMSO is proved to be an ideal green solvent when its manufacturing cost is brought down by future development.⁵⁴ More details can be found in Fig. S12 and video S2, showing the real-time dissolution of PHEMA-based OSCs.

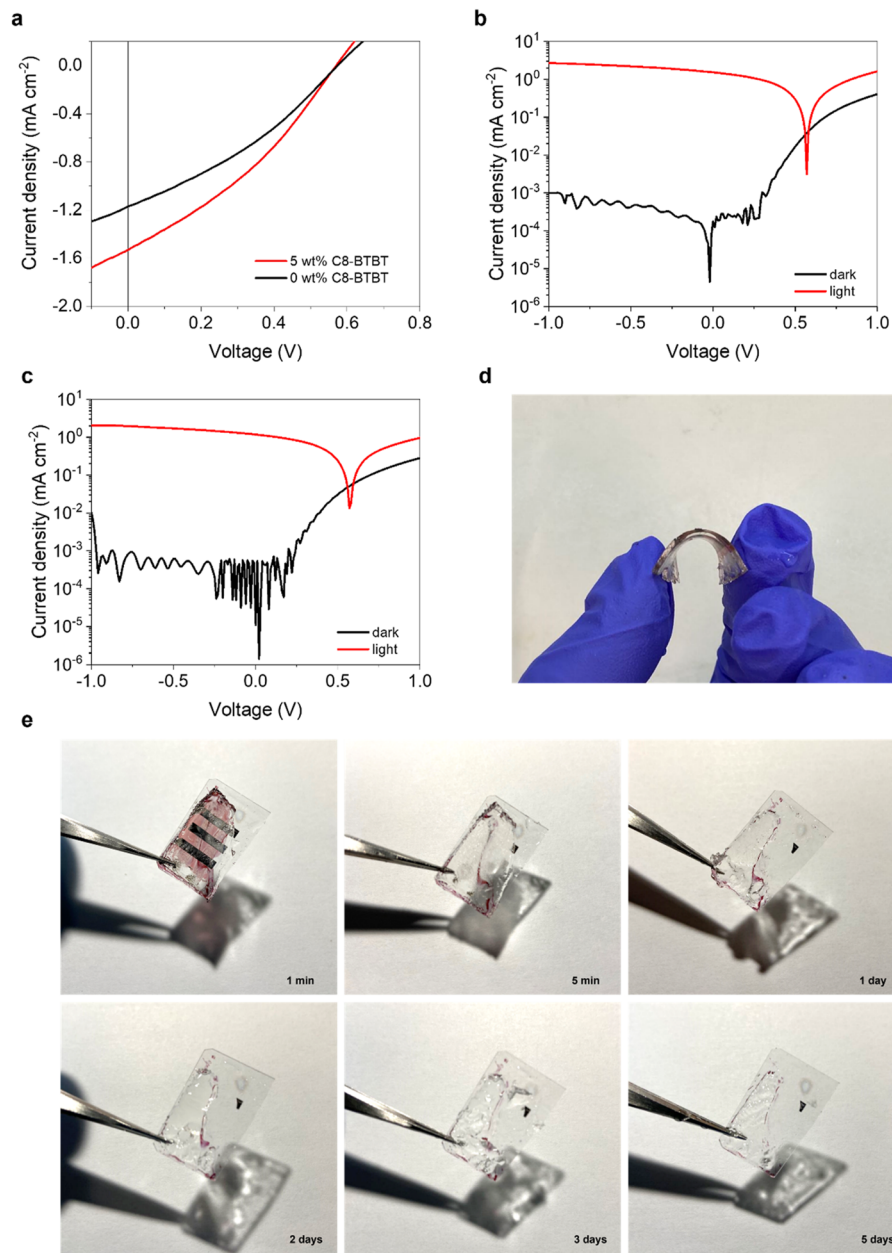


FIG. 5. (a) Linear-linear J - V characteristics of PHEMA-based OSCs with and without 5 wt. % C8-BTBT in the P3HT:PCBM active layer. (b) Log-linear light and dark J - V characteristics of PHEMA-based OSCs with 5 wt. % C8-BTBT in the P3HT:PCBM active layer. (c) Log-linear light and dark J - V characteristics of PHEMA-based OSCs with a pristine P3HT:PCBM active layer. (d) The flexibility of a PHEMA-based OSC. (e) Photographs showing the solubility of PHEMA-based OSCs using DMSO solvent. A glass slide is used for supporting the as-prepared OSCs.

IV. CONCLUSIONS

In summary, the fabrication of PHEMA hydrogel thin films by injection of precursor solution into a glass mold is optimized by adjusting the photopolymerization duration under UV light. The relationship between the wrinkle widths of the film surface and UV

exposure time is also explored. The PHMA hydrogel thin films are then used as dissolvable substrates on which organic solar cells are formed.

A smectic LC C8-BTBT has been incorporated into a P3HT:PCBM organic solar cell system to enhance the ordering of the P3HT polymer crystallization induced by thermal annealing. The

performance of the unannealed OSCs with C8-BTBT incorporation shows a clear improvement. The enhancement of device performance is confirmed to be due to the LC incorporation that promotes the crystallinity of P3HT chains. The surface morphology is also improved with C8-BTBT incorporation up to 5 wt.%. Compared with pristine P3HT:PCBM OSCs, those including C8-BTBT also exhibit distinctive optimal thermal annealing behaviors. Assessment of the photovoltaic characteristics of the fabricated OSCs reveals the evolution of various cell parameters with annealing temperature in ternary OSCs with C8-BTBT. Based on these findings, we propose that using smectic LC in ternary OSC systems provides a promising method for improving device performance.

An investigation of PHEMA film dissolvability reveals that it is linked to solvent polarity and water solubility. It is shown that PHEMA-based OSCs can be effectively disposed of by dissolving the substrate in different types of polar solvents. Using DMSO, the entire cell substrate (the bulk of a thin film solar cell) can be dissolved within 5 days. This is a promising way to achieve more bio-compatible and potentially bio-gradable OSCs.

SUPPLEMENTARY MATERIAL

Supplementary material encompass Table S1, presenting the abbreviation symbols referenced in the main text, along with Figs. S1 through S12. Figure S1 details the photopolymerization procedure of PHEMA, while Figs. S2 and S3 offer 2D images of surface morphology and POM images of C8-BTBT molecules and P3HT:PCBM:C8-BTBT thin films at gradient heating temperature, respectively. Additionally, Fig. S4 provides further POM images. Figures S5 and S6 depict UV-vis absorption spectra and X-ray diffraction patterns, while Fig. S7 showcases AFM phase images of P3HT:PCBM:C8-BTBT thin films under various C8-BTBT loading concentrations and thermal annealing temperatures. Moreover, Figs. S8 and S9 present J-V characteristics and dark semi-logarithmic plotted J-V characteristics, respectively, for P3HT:PCBM:C8-BTBT with and without pre-thermal annealing treatment. Finally, Fig. S10 illustrates the chemical structures of solvents used in the study, and Figs. S11 and S12 exhibit PHEMA dissolution results and photographs of disposable PHEMA-based OSCs using DMSO solvent.

ACKNOWLEDGMENTS

Authors acknowledge the financial support from the EPSRC SWIMS (Grant No. EP/V039717/1), Royal Society (Grant Nos. RGS\R1\221009 and IEC\NSFC\211201), and Sêr Cymru program—Enhancing Competitiveness Equipment Awards 2022–23 (Grant Nos. MA/VG/2715/22-PN66).

AUTHOR DECLARATIONS

Conflict of Interest

The authors have no conflicts to disclose.

Author Contributions

Benxuan Li: Data curation (equal); Formal analysis (equal); Investigation (equal); Writing – original draft (equal); Writing – review &

editing (equal). **Shijie Zhan:** Formal analysis (equal); Visualization (equal); Writing – review & editing (equal). **Zhe Li:** Investigation (supporting); Writing – review & editing (supporting). **Wenlong Ming:** Resources (supporting); Writing – review & editing (supporting). **Gehan A. J. Amaratunga:** Conceptualization (equal); Data curation (equal); Formal analysis (equal); Funding acquisition (equal); Investigation (equal); Methodology (equal); Project administration (equal); Resources (equal); Supervision (equal); Validation (equal); Visualization (equal); Writing – original draft (equal); Writing – review & editing (equal). **Bo Hou:** Conceptualization (lead); Data curation (lead); Formal analysis (lead); Funding acquisition (lead); Investigation (lead); Methodology (lead); Project administration (lead); Resources (lead); Supervision (lead); Validation (lead); Visualization (lead); Writing – original draft (lead); Writing – review & editing (lead).

DATA AVAILABILITY

Information on the data underpinning the results presented here, including how to access them, can be found in the Cardiff University data catalogue at <http://doi.org/10.17035/d.2024.0319961524> and in the [supplementary material](#).

REFERENCES

- 1 J. Zhao *et al.*, “Recent advances in wearable self-powered energy systems based on flexible energy storage devices integrated with flexible solar cells,” *J. Mater. Chem. A* **9**(35), 18887–18905 (2021).
- 2 J. Fu *et al.*, “19.31% binary organic solar cell and low non-radiative recombination enabled by non-monotonic intermediate state transition,” *Nat. Commun.* **14**(1), 1760 (2023).
- 3 T. H. Kim *et al.*, “Record indoor performance of organic photovoltaics with long-term stability enabled by self-assembled monolayer-based interface management,” *Nano Energy* **112**, 108429 (2023).
- 4 B. Li, B. Hou, and G. A. J. Amaratunga, “Indoor photovoltaics, the next big trend in solution-processed solar cells,” *InfoMat* **3**(5), 445–459 (2021).
- 5 R. Deng, Y. Zhuo, and Y. Shen, “Recent progress in silicon photovoltaic module recycling processes,” *Resour., Conserv. Recycl.* **187**, 106612 (2022).
- 6 J. R. Dodson *et al.*, “Bio-derived materials as a green route for precious & critical metal recovery and re-use,” *Green Chem.* **17**(4), 1951–1965 (2015).
- 7 J. M. Kadro *et al.*, “Proof-of-concept for facile perovskite solar cell recycling,” *Energy Environ. Sci.* **9**(10), 3172–3179 (2016).
- 8 C. H. Chen *et al.*, “Toxicity, leakage, and recycling of lead in perovskite photovoltaics,” *Adv. Energy Mater.* **13**(14), 2204144 (2023).
- 9 L. Sun, K. Fukuda, and T. Someya, “Recent progress in solution-processed flexible organic photovoltaics,” *Npj Flexible Electron.* **6**(1), 89 (2022).
- 10 S. J. Eichhorn *et al.*, “Current international research into cellulose as a functional nanomaterial for advanced applications,” *J. Mater. Sci.* **57**(10), 5697–5767 (2022).
- 11 M. Hassan *et al.*, “Significance of flexible substrates for wearable and implantable devices: Recent advances and perspectives,” *Adv. Mater. Technol.* **7**(3), 2100773 (2022).
- 12 K. K. Sadasivuni *et al.*, “Flexible, biodegradable and recyclable solar cells: A review,” *J. Mater. Sci.: Mater. Electron.* **30**(2), 951–974 (2019).
- 13 S. Chen *et al.*, “Biodegradable elastomers and gels for elastic electronics,” *Adv. Sci.* **9**(13), 2105146 (2022).
- 14 Y. Cao and K. E. Uhrich, “Biodegradable and biocompatible polymers for electronic applications: A review,” *J. Bioact. Compat. Polym.* **34**(1), 3–15 (2019).
- 15 Y. Zhao *et al.*, “Supramolecular adhesive hydrogels for tissue engineering applications,” *Chem. Rev.* **122**(6), 5604–5640 (2022).
- 16 W. Heng, S. Solomon, and W. Gao, “Flexible electronics and devices as human-machine interfaces for medical robotics,” *Adv. Mater.* **34**(16), 2107902 (2022).

- ¹⁷M. Kumar and S. Kumar, "Liquid crystals in photovoltaics: A new generation of organic photovoltaics," *Polym. J.* **49**(1), 85–111 (2017).
- ¹⁸S. Jeong *et al.*, "Effects of nematic liquid crystal additives on the performance of polymer solar cells," *Macromol. Chem. Phys.* **211**(23), 2474–2479 (2010).
- ¹⁹C. M. González-Henríquez *et al.*, "Fabrication of micro and sub-micrometer wrinkled hydrogel surfaces through thermal and photocrosslinking processes," *Polymer* **101**, 24–33 (2016).
- ²⁰Y.-T. Cheng *et al.*, "Improvement of organic solar cells by flexible substrate and ITO surface treatments," *Appl. Surf. Sci.* **256**(24), 7606–7611 (2010).
- ²¹J.-H. Kim *et al.*, "Flexible ITO films with atomically flat surfaces for high performance flexible perovskite solar cells," *Nanoscale* **10**(44), 20587–20598 (2018).
- ²²J. R. Meakin *et al.*, "Thermal analysis of poly (2-hydroxyethyl methacrylate)(pHEMA) hydrogels," *J. Mater. Sci.: Mater. Med.* **14**(1), 9–15 (2003).
- ²³B. Qiu *et al.*, "Highly efficient all-small-molecule organic solar cells with appropriate active layer morphology by side chain engineering of donor molecules and thermal annealing," *Adv. Mater.* **32**(21), 1908373 (2020).
- ²⁴B. Ray, P. R. Nair, and M. A. Alam, "Annealing dependent performance of organic bulk-heterojunction solar cells: A theoretical perspective," *Sol. Energy Mater. Sol. Cells* **95**(12), 3287–3294 (2011).
- ²⁵I.-C. Khoo, *Liquid Crystals* (John Wiley & Sons, 2022).
- ²⁶C. Grigoriadis *et al.*, "Order, viscoelastic, and dielectric properties of symmetric and asymmetric alkyl[1]benzothieno[3,2-b] [1]benzothiophenes," *J. Phys. Chem. B* **118**(5), 1443–1451 (2014).
- ²⁷M. Dohr *et al.*, "Reversibility of temperature driven discrete layer-by-layer formation of dioctyl-benzothieno-benzothiophene films," *Soft Matter* **13**(12), 2322–2329 (2017).
- ²⁸G. Nagarjuna *et al.*, "Tuning aggregation of poly(3-hexylthiophene) within nanoparticles," *ACS Nano* **6**(12), 10750–10758 (2012).
- ²⁹O. Oklobia and T. Shafai, "A study of donor/acceptor interfaces in a blend of P3HT/PCBM solar cell: Effects of annealing and PCBM loading on optical and electrical properties," *Solid-state Electron.* **87**, 64–68 (2013).
- ³⁰F. C. Spano, "Modeling disorder in polymer aggregates: The optical spectroscopy of regioregular poly(3-hexylthiophene) thin films," *J. Chem. Phys.* **122**(23), 234701 (2005).
- ³¹T. Erb *et al.*, "Absorption and crystallinity of poly(3-hexylthiophene)/fullerene blends in dependence on annealing temperature," *Thin Solid Films* **511–512**, 483–485 (2006).
- ³²G. Louarn *et al.*, "Raman spectroscopic studies of regioregular poly(3-alkylthiophenes)," *J. Phys. Chem.* **100**(30), 12532–12539 (1996).
- ³³A. Ruseckas *et al.*, "Intra- and interchain luminescence in amorphous and semicrystalline films of phenyl-substituted polythiophene," *J. Phys. Chem. B* **105**(32), 7624–7631 (2001).
- ³⁴W. Barford, "Exciton transfer integrals between polymer chains," *J. Chem. Phys.* **126**(13), 134905 (2007).
- ³⁵Y. Kim *et al.*, "A strong regioregularity effect in self-organizing conjugated polymer films and high-efficiency polythiophene:fullerene solar cells," *Nat. Mater.* **5**(3), 197–203 (2006).
- ³⁶L. H. Nguyen *et al.*, "Effects of annealing on the nanomorphology and performance of poly(alkylthiophene):fullerene bulk-heterojunction solar cells," *Adv. Funct. Mater.* **17**(7), 1071–1078 (2007).
- ³⁷Z. Wang *et al.*, "Marangoni effect-controlled growth of oriented film for high performance C8-BTBT transistors," *Adv. Mater. Interfaces* **6**(8), 1801736 (2019).
- ³⁸M. Campoy-Quiles *et al.*, "Morphology evolution via self-organization and lateral and vertical diffusion in polymer:fullerene solar cell blends," *Nat. Mater.* **7**(2), 158–164 (2008).
- ³⁹I.-W. Hwang, D. Moses, and A. J. Heeger, "Photoinduced carrier generation in P3HT/PCBM bulk heterojunction materials," *J. Phys. Chem. C* **112**(11), 4350–4354 (2008).
- ⁴⁰F. E. Osterloh *et al.*, "P3HT:PCBM bulk-heterojunctions: Observing interfacial and charge transfer states with surface photovoltage spectroscopy," *J. Phys. Chem. C* **118**(27), 14723–14731 (2014).
- ⁴¹M. Zhu *et al.*, "Interfacial chemical and electronic structure of cobalt deposition on 2,7-dioctyl[1]benzothieno[3,2-b]benzothiophene (C8-BTBT)," *Appl. Surf. Sci.* **402**, 142–146 (2017).
- ⁴²F. Padinger, R. S. Rittberger, and N. S. Sariciftci, "Effects of postproduction treatment on plastic solar cells," *Adv. Funct. Mater.* **13**(1), 85–88 (2003).
- ⁴³X. Yang *et al.*, "Nanoscale morphology of high-performance polymer solar cells," *Nano Lett.* **5**(4), 579–583 (2005).
- ⁴⁴K. Tvingstedt and C. Deibel, "Temperature dependence of ideality factors in organic solar cells and the relation to radiative efficiency," *Adv. Energy Mater.* **6**(9), 1502230 (2016).
- ⁴⁵M.-H. Jao, H.-C. Liao, and W.-F. Su, "Achieving a high fill factor for organic solar cells," *J. Mater. Chem. A* **4**(16), 5784–5801 (2016).
- ⁴⁶S. Yoo, B. Domercq, and B. Kippelen, "Intensity-dependent equivalent circuit parameters of organic solar cells based on pentacene and C60," *J. Appl. Phys.* **97**(10), 103706 (2005).
- ⁴⁷A. De Vos, "The fill factor of a solar cell from a mathematical point of view," *Solar Cells* **8**(3), 283–296 (1983).
- ⁴⁸B. Jung *et al.*, "Sustainable system for raw-metal recovery from crystalline silicon solar panels: From noble-metal extraction to lead removal," *ACS Sustainable Chem. Eng.* **4**(8), 4079–4083 (2016).
- ⁴⁹J. Wang, W. Wu, and Z. Lin, "Kinetics and thermodynamics of the water sorption of 2-hydroxyethyl methacrylate/styrene copolymer hydrogels," *J. Appl. Polym. Sci.* **109**(5), 3018–3023 (2008).
- ⁵⁰F. Machui *et al.*, "Determination of the P3HT:PCBM solubility parameters via a binary solvent gradient method: Impact of solubility on the photovoltaic performance," *Sol. Energy Mater. Sol. Cells* **100**, 138–146 (2012).
- ⁵¹M. Rawat *et al.*, "Organic solar cells on paper substrates," *Adv. Mater. Technol.* **4**(8), 1900184 (2019).
- ⁵²F. J. Weber and J. A. de Bont, "Adaptation mechanisms of microorganisms to the toxic effects of organic solvents on membranes," *Biochim. Biophys. Acta, Rev. Biomembr.* **1286**(3), 225–245 (1996).
- ⁵³N. Espinosa *et al.*, "Large scale deployment of polymer solar cells on land, on sea and in the air," *Energy Environ. Sci.* **7**(3), 855–866 (2014).
- ⁵⁴S. U. Hong *et al.*, "Are green solvents truly green? Integrating life cycle assessment and techno-economic analysis for sustainable membrane fabrication," *Green Chem.* **25**(11), 4501–4512 (2023).
- ⁵⁵H. J. Heipieper *et al.*, "Mechanisms of resistance of whole cells to toxic organic solvents," *Trends Biotechnol.* **12**(10), 409–415 (1994).